Supplementary Information: White light diffraction tomography of unlabeled live cells

Taewoo Kim[1†], Renjie Zhou[1,2†], Mustafa Mir[1], S. Derin Babacan[3], P. Scott Carney[4], Lynford L. Goddard[2], and Gabriel Popescu[1]*

*[*gpopescu@illinois.edu](mailto:gpopescu@illinois.edu)

a. Spatial light interference microscopy (SLIM)

Spatial light interference microscopy (SLIM)[1] is a recently developed quantitative phase imaging technique, which combines Zernike's phase contrast microscopy and Gabor's holography. It is capable of measuring nanoscale structures and dynamics in live cells by generating endogenous contrast and mapping quantitative optical path-lengths at each point in the image. Figure S1a shows a schematic for the SLIM experimental setup, which is designed to be an add-on module to a commercial phase contrast microscope (Axio Observer Z1). This microscope has a motorized focus drive with a minimum step size of 10 nm and an F/0.55 motorized shutter that allows us precise z-scanning and illumination control. The back focal plane of the objective lens contains a thin metal annulus (phase ring) which provides a $\pi/2$ phase shift between the scattered and unscattered light. In SLIM, the image plane of the phase contrast microscope is first relayed and magnified through a 4*f* system (AC508-150-A1-ML 150mm doublet and AC508-200-A1-ML 200mm doublet, Thorlabs), and the back focal plane of the objective lens is imaged onto a programmable liquid crystal spatial light modulator (XY Phase Series Model P512 -635, Boulder Nonlinear Systems, Inc, USA), which is located in the Fourier plane of the second 4*f* system (AC508-300-A1-ML 300mm doublet and AC508-500-A1-ML 500mm doublet, Thorlabs). A desired ring pattern is projected onto the SLM, and is matched to the image of the ring on the SLM. In this manner the SLM is used to provide additional phase shifts of 0, $\pi/2$, π and $3\pi/2$ between the scattered and un-scattered light. These four phase shifted interferograms are recorded at the image plane (at the focus of the second Fourier lens) using a CCD detector (AxioCam MRm, Zeiss). The SLM, CCD, and microscope are synchronized through a custom LabVIEW program. In SLIM we acquire 8 fps, which translates to 2 quantitative phase images (QPI) per second. This acquisition rate is limited by the frame rate of the CCD and the refresh rate of SLM. Therefore, for example, a z-stack of 100 slices can be obtained in 50 seconds. By using these four interferograms, the actual phase shift caused by the sample can be uniquely determined within a range of 2π. Any 2π ambiguities are corrected by Goldstein's unwrapping algorithm.

The broadband source (12V, 100W Hal, square filament, Zeiss) with a temporal coherence length of 1.2μm takes a significant role in increasing resolution since it does not suffer from speckle, and thus, improves the sensitivity (0.029nm temporal and 0.28nm spatial sensitivities). Also, since SLIM is built as an add-on module to a commercial microscope, it is possible to overlay SLIM with other microscopy modalities (e.g. epi-fluorescence, DIC). With these features, SLIM is capable of performing multimodal and functional studies[2-9]. Furthermore, with the short coherence length and a high numerical aperture objective, SLIM provides excellent depth

sectioning (1.2 µm depth sectioning for a 63x/1.4NA objective), which plays a large role in our reconstruction method.
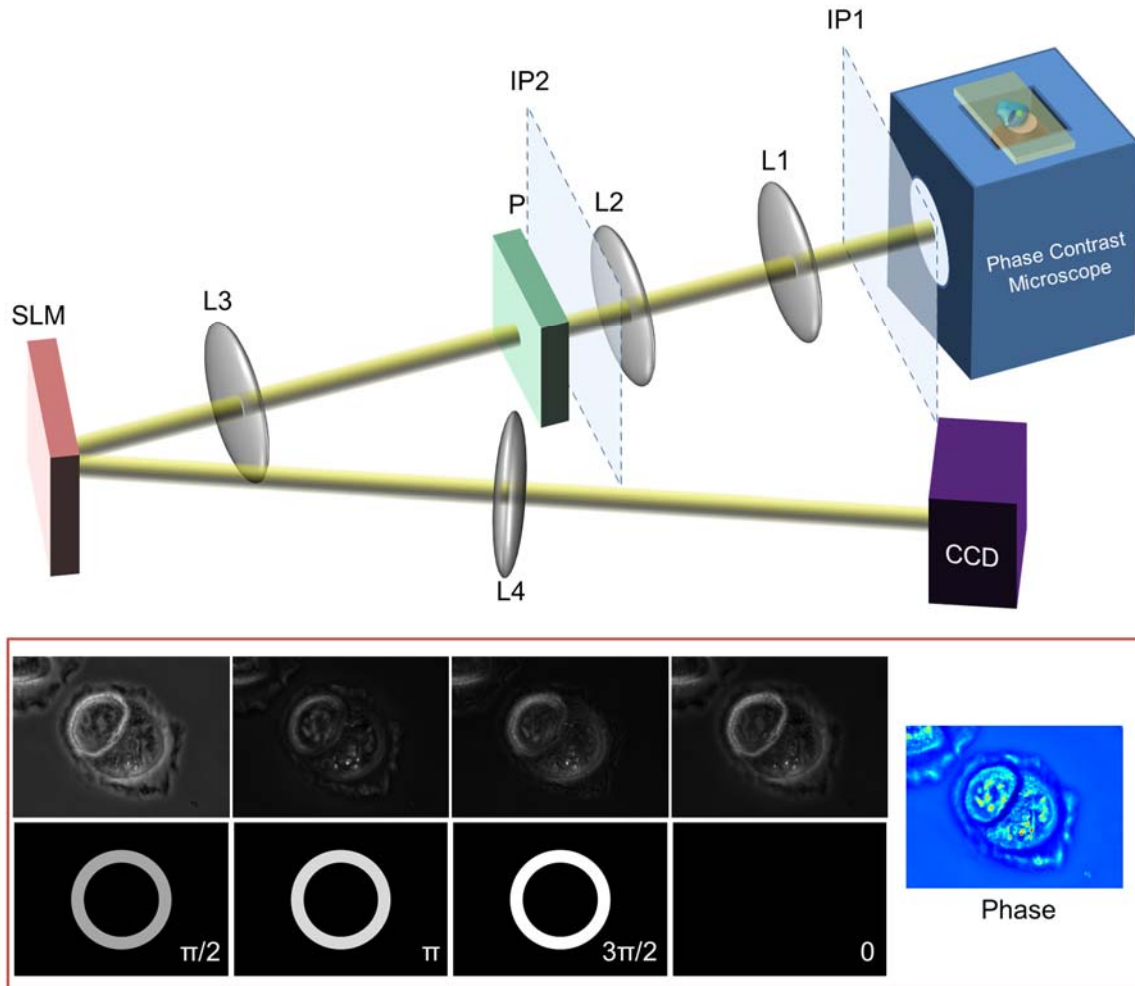
Figure S1. Illustration the SLIM module and the phase image measurement. (top) A schematic of SLIM setup built as an add-on module to a commercial phase contrast microscope. L1 (f = 150mm) and L2 (f = 200mm) forms a 4f system, which relays the image plane of the microscope (IP1) to a new image plane (IP2) so that the modulation at the spatial light modulator (SLM) can be optimized. The polarizer (P) aligns the polarization of the field with the slow axis of the SLM. L3 (f = 300mm) and L4 (f = 500mm) forms another 4f system, where the SLM is at the Fourier plane and the CCD is at the relayed image plane. (bottom) 4 different phase shifted images shown with the illustrations of corresponding phase pattern on the SLM. SLIM measures the phase of the object by combining these four frames.

Here we provide additional explanation of SLIM's imaging principle. We first define the temporal cross-correlation function, $\Gamma_{12}(\mathbf{r},\tau)$, as[9, 10]

$$\Gamma_{12}(\mathbf{r},\tau) = \left\langle U_s(\mathbf{r},t)U_r^*(\mathbf{r},t+\tau)\right\rangle, \qquad (a1)$$

where U_s and U_r are the scattered and the reference (unscattered) field, respectively. $\Gamma_{12}(\mathbf{r},\tau)$ is a complex function that can be written as

$$\Gamma_{12}(\mathbf{r},\tau)=\left|\Gamma_{12}(\mathbf{r},\tau)\right|e^{i\phi(\mathbf{r},\tau)}, \tag{a2}$$

where $\phi(\mathbf{r},\tau)$ is the phase associated with the image field, which we measure in SLIM using the four phase shifted interferograms. The generalized Wiener-Khintchine theorem[10, 11] allows us to relate $\Gamma_{12}(\mathbf{r},\tau)$ to the cross-spectral density through Fourier transform of

$$\Gamma_{12}(\mathbf{r},\tau)=\int_0^\infty W_{12}(\mathbf{r},\omega)e^{i\omega\tau}d\omega, \tag{a3}$$

where

$$W_{12}(\mathbf{r},\omega)=\left\langle U_s(\mathbf{r},\omega)U_r^*(\mathbf{r},\omega)\right\rangle. \tag{a4}$$

During the phase shifting measurement, $\Gamma_{12}(\mathbf{r},\tau)$ is evaluated at $\tau=0$, which allows us to write

$$\Gamma_{12}(\mathbf{r},\tau=0)=\int_0^\infty\left\langle U_s(\mathbf{r},\omega)U_r^*(\mathbf{r},\omega)\right\rangle d\omega. \tag{a5}$$

We see from Eq. (a5) that the unknown quantity is the scattered field, U_s. In the next section, we first derive an analytical solution for U_s and then establish the relationship between the measurable quantity, Γ_{12}, and the 3D object structure of interest.

b. White light diffraction tomography (WDT)

The inhomogeneous Helmholtz equation, which describes the field U in a medium with index distribution of $n(\mathbf{r})$ is

$$\nabla^2 U(\mathbf{r},\omega)+n^2(\mathbf{r},\omega)\beta_0^2(\omega)U(\mathbf{r},\omega)=0, \tag{b1}$$

where $\beta_0(\omega)=\omega/c$ is the wavenumber in vacuum. We re-arrange Eq. (b1) as

$$\nabla^2 U(\mathbf{r},\omega)+\beta^2(\omega)U(\mathbf{r},\omega)=-\chi(\mathbf{r},\omega)\beta_o^2(\omega)U(\mathbf{r},\omega), \tag{b2}$$

where $\beta(\omega)=\bar{n}\beta_0(\omega)$ (we assume non-dispersive objects), $\bar{n}=\left\langle n(\mathbf{r})\right\rangle_r$ is the spatially averaged refractive index, and $\chi(\mathbf{r},\omega)=n^2(\mathbf{r},\omega)-\bar{n}^2(\omega)$ is the scattering potential. The total field $U(\mathbf{r},\omega)$ can be written as $U(\mathbf{r},\omega)=U_i(\mathbf{r},\omega)+U_s(\mathbf{r},\omega)$, where $U_i(\mathbf{r},\omega)$ is the incident wave. U_i satisfies the homogeneous wave equation,

$$\nabla^2 U_i(\mathbf{r},\omega)+\beta^2(\omega)U_i(\mathbf{r},\omega)=0. \tag{b3}$$

Equation (b3) has a plane-wave solution $U_i(\mathbf{r},\omega)=A(\omega)e^{i\beta(\omega)z}$ where $A(\omega)$ is the spectral amplitude of the incident field. Subtracting Eq. (b2) from Eq. (b3) gives

$$\nabla^2 U_s(\mathbf{r},\omega)+\beta^2(\omega)U_s(\mathbf{r},\omega)=-\chi(\mathbf{r})\beta_o^2(\omega)U(\mathbf{r},\omega). \tag{b4}$$

From Eq. (b4) we can clearly see that the driving term of the right hand side represents the interaction of the object scattering potential χ with the total field U. Under the first Born approximation, i.e., $\left|U_s\left(\mathbf{r},\omega\right)\right| << \left|U_i\left(\mathbf{r},\omega\right)\right|$, we can approximate $U\left(\mathbf{r},\omega\right)$ on the right hand side as $U_i\left(\mathbf{r},\omega\right)$, allowing Eq. (b4) to be re-written as,

$$\nabla^2 U_s\left(\mathbf{r},\omega\right) + \beta^2\left(\omega\right) U_s\left(\mathbf{r},\omega\right) = -\chi\left(\mathbf{r},\omega\right)\beta_o^2\left(\omega\right) A\left(\omega\right) e^{i\beta(\omega)z} . \qquad \text{(b5)}$$

Instead of employing the traditional Green's function approach and the angular spectrum representation (Weyl's formula), we solve for the scattered field directly in the wavevector space, using the 3D Fourier transformation. We first perform a 3D Fourier transform of Eq. (b5), which yields

$$\left[\beta^2\left(\omega\right) - k^2\right] U_s\left(\mathbf{k},\omega\right) = -\beta_0^2\left(\omega\right) A\left(\omega\right) \chi\left[\mathbf{k}_\perp, k_z - \beta\left(\omega\right)\right] . \qquad \text{(b6)}$$

In Eq. (b6), we used the *shift theorem* of Fourier transforms, namely, $\chi\left(\mathbf{r},\omega\right) e^{i\beta(\omega)z} \to \chi\left[\mathbf{k}_\perp, k_z - \beta\left(\omega\right)\right]$, where the arrow indicates Fourier transformation. Note that, throughout the manuscript, we use the same symbol for a function and its Fourier transform but carry all the arguments explicitly, which clearly identifies the domain in which the function operates. For example, $\chi\left(\mathbf{k}\right)$ is the Fourier transform of $\chi\left(\mathbf{r}\right)$.

From Eq. (b6), the scattered field U_s is obtained immediately,

$$U_s\left(\mathbf{k},\omega\right) = -\beta_0^2\left(\omega\right) A\left(\omega\right) \frac{\chi\left[\mathbf{k}_\perp, k_z - \beta\left(\omega\right)\right]}{\beta^2\left(\omega\right) - k_\perp^2 - k_z^2} . \qquad \text{(b7)}$$

Next, we derive an expression for the field as a function of axial distance z, i.e., we arrange the terms such that a 1D inverse Fourier transform with respect to k_z can be easily performed. Toward this end, we define a $k_\perp$-dependent propagation constant, $q = \sqrt{\beta^2\left(\omega\right) - k_\perp^2}$, and re-write Eq. (b7) as

$$U_s\left(\mathbf{k},\omega\right) = -\beta_0^2\left(\omega\right) A\left(\omega\right) \chi\left[\mathbf{k}_\perp, k_z - \beta\left(\omega\right)\right] \frac{1}{2q}\left(\frac{1}{k_z - q} - \frac{1}{k_z + q}\right) . \qquad \text{(b8)}$$

Since our imaging experiment only measures the transmitted field or the forward scattered field, we ignore the backscattered field, $\frac{1}{k_z + q}$. We perform an inverse Fourier transform on Eq. (b8) with respect to k_z in order to obtain the forward scattered field as a function of transverse wavevector, $\mathbf{k}_\perp$, axial distance, z, and angular frequency, ω

$$U_s\left(\mathbf{k}_\perp, z; \omega\right) = -\frac{\beta_0^2\left(\omega\right) A\left(\omega\right)}{2q}\left[\chi\left(\mathbf{k}_\perp, z\right) e^{i\beta(\omega)z}\right] \circledv_z e^{iqz} . \qquad \text{(b9)}$$

In Eq. (b9), $\bigcirc_z$ indicates convolution along the z-dimension, $f(z)\bigcirc_z e^{iqz} = \int\limits_{-\infty}^{\infty} f(z')e^{iq(z-z')}dz'$. It can

be easily seen that the convolution of a function with a complex exponential yields the Fourier transform of that function multiplied the complex exponential, which yields the simple result $\left[\chi(\mathbf{k}_\perp, z; \omega)e^{i\beta(\omega)z}\right]\bigcirc_z e^{iqz} = e^{iqz}\chi\left[\mathbf{k}_\perp, q-\beta(\omega)\right]$.

In order to insert the result of Eq. (b9) into Eq. (a5), we need to Fourier transform $\Gamma_{12}(\mathbf{r}, \tau)$ with

respect to the transverse position vector, $\mathbf{r}_\perp = (x, y)$. Since $U_r(\mathbf{r}, \omega)$ is a plane wave propagating

in z-direction, Eq. (a4) in $\mathbf{k}_\perp$-space is

$$W_{12}(\mathbf{k}_\perp, z, \omega) = \left\langle U_s(\mathbf{k}_\perp, z, \omega)U_r^*(z, \omega)\right\rangle. \qquad (b10)$$

Using the solution of U_s from Eq. (b9) and $U_r(z, \omega) = A(\omega)e^{i\beta(\omega)z}$, we have

$$W_{12}(\mathbf{k}_\perp, z, \omega) = \frac{-\beta_o^2(\omega)S(\omega)e^{iz[q-\beta(\omega)]}}{2q}\chi\left[\mathbf{k}_\perp, q-\beta(\omega)\right], \qquad (b11)$$

where $S(\omega) = |A(\omega)|^2$ is the power spectrum of the illumination field. Using Eq. (a5) we obtain

the temporal cross correlation at zero-delay as a function of the frequency integral

$$\Gamma_{12}(\mathbf{k}_\perp, z, 0) = -\int\limits_0^{\infty}\frac{\beta_o^2(\omega)S(\omega)e^{iz[q-\beta(\omega)]}}{2q}\chi\left[\mathbf{k}_\perp, q-\beta(\omega)\right]d\omega. \qquad (b12)$$

With the relation $\beta(\omega) = \overline{n}\beta_0 = \overline{n}\omega/c$, we can change the integral from $d\omega$ to $d\beta$, $S(\omega)$ to

$S(\beta c/\overline{n})$, such that Eq. (b12) becomes

$$\Gamma_{12}(\mathbf{k}_\perp, z, 0) = -\frac{c}{2\overline{n}^3}\int\limits_0^{\infty}\frac{\beta^2 S(\beta c/\overline{n})e^{iz(q-\beta)}}{q}\chi(\mathbf{k}_\perp, q-\beta)d\beta. \qquad (b13)$$

Experimentally, we measure $S(\lambda)$. So to obtain the spectrum distribution for $S(\beta c/\overline{n})$ from

$S(\lambda)$, we need to consider the Jacobian transformations, $S(\beta c/\overline{n}) \leftrightarrow \overline{n}S(\beta)/c$ and

$S(\beta) \leftrightarrow \lambda^2 S(\lambda)/2\pi$. In order to evaluate the integral in Eq. (b13), we define a new variable

$Q = q - \beta = \sqrt{\beta^2 - k_\perp^2} - \beta$, from which we have $\beta = -\frac{Q^2 + k_\perp^2}{2Q}$ and $q = \left(-\frac{Q}{2} + \frac{k_\perp^2}{2Q}\right)$. Substituting

$d\beta$ for dQ, we need to consider the Jacobian $\frac{d\beta}{dQ} = \left(-\frac{1}{2} + \frac{k_\perp^2}{2Q^2}\right)$, then Eq. (b13) becomes

$$\Gamma_{12}(\mathbf{k}_\perp, z; 0) = \frac{1}{8\overline{n}^2} \int_0^\infty \frac{(Q^2 + k_\perp^2)^2}{Q^3} S\left(-\frac{Q^2 + k_\perp^2}{2Q}\right) \chi(\mathbf{k}_\perp, Q) e^{izQ} dQ$$

$$= \frac{1}{8\overline{n}^2} FT_Q^{-1} \left[\frac{(Q^2 + k_\perp^2)^2}{Q^3} S\left(-\frac{Q^2 + k_\perp^2}{2Q}\right) \right] \circledcirc_z \chi(\mathbf{k}_\perp, -z). \qquad \text{(b14)}$$

$$= \Sigma(\mathbf{k}_\perp, -z) \circledcirc_z \chi(\mathbf{k}_\perp, -z)$$

In Eq. (b14), Σ is the function that incorporates all the details of the instrument response. Note that the $\mathbf{k}_\perp$ coverage of Σ is limited to a maximum value $\mathbf{k}_\perp^{\text{max}} = \beta_0 NA$, where NA is the numerical aperture of the objective. By measuring z-stacks in SLIM, we can reconstruct the object's 3D distribution through deconvolution of Eq. (b14). Alternatively, we can write Eq. (b14) in the spatial frequency domain as a product, namely,

$$\Gamma_{12}(\mathbf{k}_\perp, Q; 0) = \Sigma(\mathbf{k}_\perp, Q) \chi(\mathbf{k}_\perp, Q), \qquad \text{(b15)}$$

where,

$$\Sigma(\mathbf{k}_\perp, Q) = \frac{1}{8\overline{n}^2} \frac{(Q^2 + k_\perp^2)^2}{Q^3} S\left(-\frac{Q^2 + k_\perp^2}{2Q}\right). \qquad \text{(b16)}$$

c. Point spread function calculation

Notice that Eq. (b16) gives the *coherent transfer function* or the Fourier transform of the point spread function (PSF) of the imaging system. Therefore, by measuring the source spectrum and filtering according to the NA of the objective, the coherent transfer function of the system can be calculated directly.
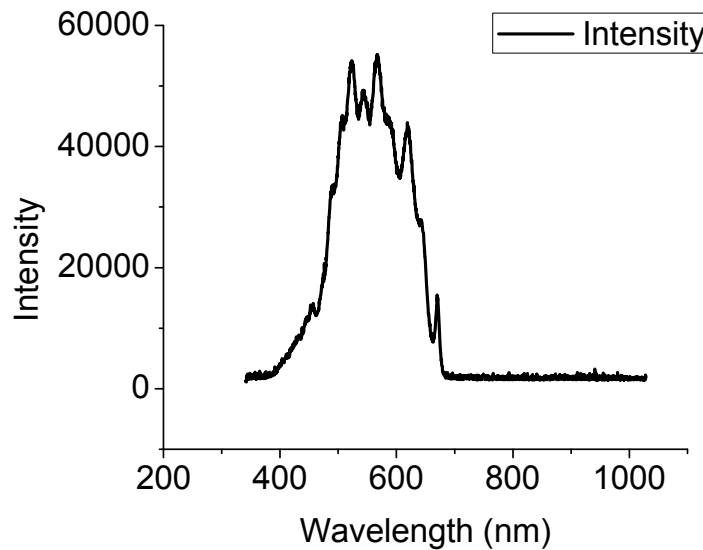
Figure S2. Spectrum of the white light source for SLIM, measured over the range of 340nm to 1028nm. The y-axis is in arbitrary units.

First, the optical spectrum (Fig. S2) of the lamp (12V, 100W Hal, square filament, Zeiss) is measured at 3200K using a fiber optic spectrometer (Ocean Optics USB2000+ Fiber Optic Spectrometer). Since the spectrum is measured as $S(\lambda)$ in air, we perform the Jacobian transformation introduced in the previous section to obtain the spectrum in terms of variable $\beta = -\left(Q^2 + k_\perp^2\right)\big/2Q$. Next through numerical calculations, this spectrum is resampled onto a 3D grid in spatial-frequency space (k_x, k_y, Q). For a 63x/1.4NA objective, each pixel in space corresponds to 45 nm and each z-slice is separated by 200 nm. Because of the quadratic relationship between Q and β, the resampling yields two duplicates of the spectrum. Therefore, the second of the two duplicates which appears at high Q is removed by applying a spatial low-pass filter with cutoff $Q = k_\perp$. Further filtering in Q is performed to incorporate the physical minimum and maximum value of Q and the maximum $k_\perp$ value, which is determined by the NA of the objective, $k_\perp^{\max} = \beta_0 NA$. In order to avoid well known numerical artifacts due to sharp cutoffs in the frequency domain, we used a simple apodization procedure to smooth the edges of the filter function. Thus, we convolved the filter function with a narrow Gaussian function, of a width that is 5% of the system's maximum transverse frequency, $k_\perp^{\max}$. Finally, the coherent transfer function (shown in Figs. 2b-c), is Fourier transformed to obtain the PSF. Figures S3a-b show the phase of the complex PSF (top row from WDT, middle row from measurement, and bottom row from deconvolving the measurement with the PSF from WDT), which was normalized and thresholded to suppress side lobes. This complex PSF was used for the 3D reconstruction, as detailed below.

d. Deconvolution algorithm

SLIM measures the 3D complex field distribution, i.e. phase and amplitude, which can be expressed as a convolution between the point spread function (PSF) of the imaging system, $\Sigma(\mathbf{r})$, and the structure of the object, $\chi(\mathbf{r}) = n^2(\mathbf{r}) - \bar{n}^2$. We represent the real field as a complex analytic signal, $\bar{U}(\mathbf{r}) = \chi(\mathbf{r}) \circledcirc \Sigma(\mathbf{r}) + \zeta(\mathbf{r})$, which also contains a signal independent noise term, $\zeta(\mathbf{r})$. Considering a weakly scattering phase object with very small absorption, where most of the useful information is contained in the phase image, it is reasonable to assume that the amplitude of the field is constant over the entire space. Therefore, the deconvolution can be performed on the phase term only, $\exp\left[i\Phi(\mathbf{r})\right]$. The function that our algorithm minimizes is

$$\hat{\Phi}(\mathbf{r}) = \arg\min_{\Phi(\mathbf{r})} \frac{1}{2\sigma^2} \left\| \exp\left[i\bar{\Phi}(\mathbf{r})\right] - \Sigma(\mathbf{r}) \circledcirc \exp\left[i\Phi(\mathbf{r})\right] \right\|^2 + \rho R\left[\Phi(\mathbf{r})\right] \qquad (\text{d1})$$

where σ^2 is the noise variance, ρ is the regularization parameter, and R is the regularization functional. For simplification, these purely phase-dependent fields can be expressed in vector forms.

$$\hat{\mathbf{f}} = \arg\min_{\mathbf{f}} \frac{1}{2\sigma^2} \|\mathbf{g} - \mathbf{\Sigma}\mathbf{f}\|^2 + \rho R(\mathbf{f}) \qquad (d2)$$

where $\mathbf{g}$ represents the measured field, $\exp\left[i\bar{\Phi}(\mathbf{r})\right]$, $\mathbf{f}$ represents the unknown field from the structure, $\exp\left[i\Phi(\mathbf{r})\right]$, and $\mathbf{\Sigma}$ represents the convolution matrix corresponding to the PSF.

Phase contrast (PC) images are highly sensitive to the sharp object boundaries, but not to slow variations in the background region. For small scale objects, such as a biological cell, these characteristics of PC allows us to use the sparse representation[12], which has been used to solve a number of imaging problems[3, 13, 14], and also has been shown to generally have superior performance to classical deconvolution methods[13, 15]. When an appropriate transform is applied to a phase image, only a few of the transform coefficients contain most of the signal energy while all the other coefficients become very small. This situation is known as *transform sparsity*. In our work, the first- and second-order directional difference operators, $\begin{bmatrix} -1 & 1 \end{bmatrix}$ and $\begin{bmatrix} -1 & 2 & -1 \end{bmatrix}$, along with 45° and -45° first-order derivative filters, $\begin{bmatrix} -1 & 0 \\ 0 & 1 \end{bmatrix}$ and $\begin{bmatrix} 0 & -1 \\ 1 & 0 \end{bmatrix}$, are used as transforms. For each plane in the image, *x-y*, *y-z* and *z-x*, these 2D transforms are applied and total of 12 transforms are generated to hold the spatial variations. Therefore, by applying the sparse deconvolution principle with these filters, the problem in Eq. (d2) can be expressed as

$$\hat{\mathbf{f}}, \hat{\alpha}_{ki} = \arg\min_{\mathbf{f}, \alpha_{ki}} \frac{1}{\sigma^2} \|\mathbf{g} - \mathbf{\Sigma}\mathbf{f}\|^2 + \sum_k (\mathbf{D}_k\mathbf{f})^T \mathbf{A}_k (\mathbf{D}_k\mathbf{f}) \qquad (d3)$$

where α_{ki} are the weighting coefficients for each plane, i, $\mathbf{D}_k$ are the transform matrices, and $\mathbf{A}_k$ are diagonal matrices with α_{ki} in the diagonal. This problem is solved by an alternating iterative minimization scheme where only one unknown is estimated at a time while others are fixed. As a result, the complex image $\mathbf{f}$ is estimated by taking derivative of Eq. (d3) and setting it to zero. Therefore, the solution is of the structure is,
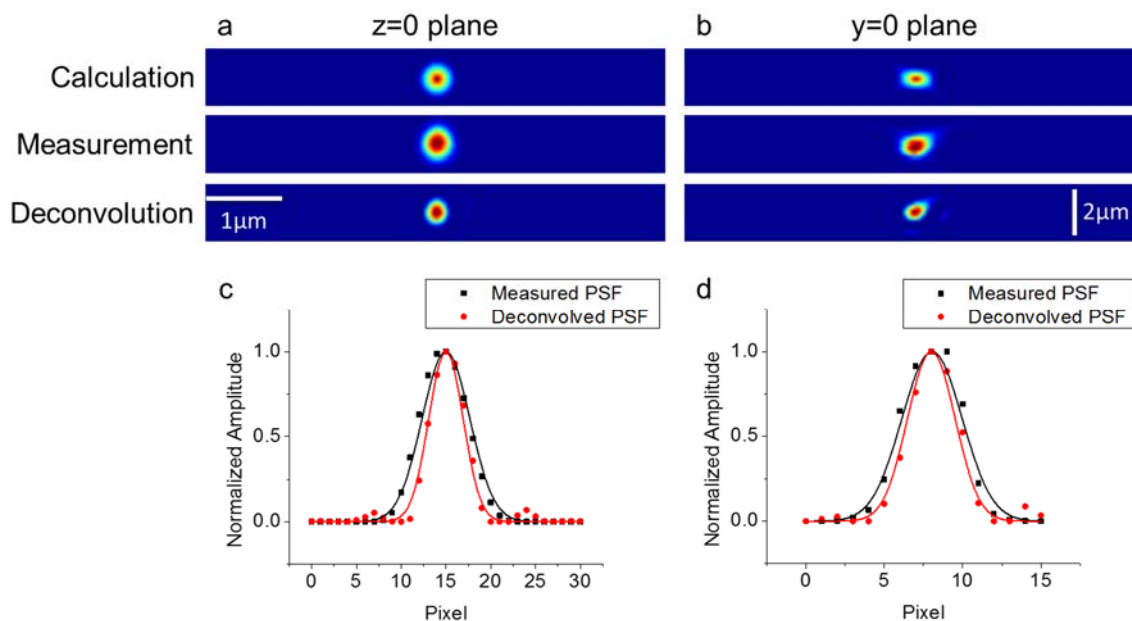
$$\hat{\mathbf{f}} = \left(\mathbf{\Sigma}^T\mathbf{\Sigma} + \sigma^2 \sum_k \mathbf{D}_k^T \mathbf{A}_k \mathbf{D}_k \right)^{-1} \mathbf{\Sigma}^T \mathbf{g} \qquad (d4)$$

and the weighting coefficients are estimated to be,

$$\hat{\alpha}_{ki} = \frac{1}{\left|(\mathbf{D}_k\hat{\mathbf{f}})\right|_i^2 + \varepsilon} \qquad (d5)$$

where ε is a small number (10^{-9} in our case) used to avoid the trivial solution.

Figure S3. Point spread function profiles and resolution improvement. (a) Point spread function in the z=0 plane, showing the calculated result, measurement, and the deconvolved measured PSF using the calculated PSF. (b) Point spread function in the y=0 plane, showing the calculated result, measurement, and the deconvolved measured PSF using the calculated PSF. (c) Profile of the measured PSF and the deconvolved PSF in x-direction, which shows FWHM decrease from 398nm to 285nm. (d) Profile of the measured PSF and the deconvolved PSF in z-direction, which shows FWHM decrease from 1218nm to 967nm.

Using this approach, first a deconvolution of the measured point spread function is performed using the theoretical PSF corresponding to the 63x/1.4NA Oil Ph3 M27 objective. In the ideal case, the resolution gain should be very high so that the deconvolved PSF essentially reaches a spatial delta function. However, because of the differences between the measured PSF and theoretical PSF which comes from the lack of incorporation of errors and aberrations, the resolution gain is 1.39x in the transverse dimension (FWHM decreases from 398nm to 285nm) and 1.26x in the vertical dimension (FWHM decreases from 1218nm to 967nm). Figure S3 illustrates this increase in resolution.

For the red blood cell in Fig. 3, which is measured with a 40x/0.75NA phase contrast objective, a new PSF is calculated for deconvolution and the deconvolution is performed on a z-stack image of 128x128x100 pixels. The deconvolution process took approximately 5 minutes. The E. Coli cell reconstruction in Fig. 4 was obtained using the PSF for the 63x/1.4NA objective and a z-stack image of 128x128x17pixels, which took approximately 3 minutes for deconvolution. Due to the large size of the z-stack 640x640x140 for the HT29 cell in Fig. 5, we first split the original z-stack into 5x5 smaller z-stacks (192x192x140), each padded with 32 zero-valued pixels on each side to increase spatial sampling. For each smaller z-stack, the sparse deconvolution is applied using the 63x/1.4NA PSF. Overall, the deconvolution process for all 25 stacks took approximately one hour. Then the center region (128x128x140) of each z-stack is obtained, renormalized, and stitched together to obtain the full deconvolved image.

e. 3D rendering

For Figs. 2b, 3b and 4c, specific color schemes are used so that the background of the image where the value of 0 corresponds to black. Then the 3D rendering is done in ImageJ with ImageJ 3D viewer plug-in using a sampling rate of 1. For Fig. 5c, each slice in the z-stack is false-colored depending on the spatial separation and the gray value of each structure and then merged back together to one z-stack. Again, 3D rendering is done in ImageJ with the ImageJ 3D viewer plug-in using a sampling rate of 1.

f. Cell preparation and imaging

E. coli MG1655 cells are cultured in Luria Broth and then sub-cultured by 100x dilution into commercial M9CA media with Thiamine (Teknova M8010) until they reach an optical density of ~0.2. The cells are then concentrated to an optical density of ~0.4 and 2 μL of the culture is pipetted onto a glass bottom dish (In Vitro Scientific D29-21-1-N) and covered by a 1mm thick agar slab (1.5% Agarose, M9CA media). In order to mitigate drying of the agar, 70 μL of H_2O is carefully pipetted onto the edge of the dish, ensuring that it never makes contact with the sample. The dish is then covered with a circular coverslip to reduce the effects of evaporation.

Human colon adenocarcinoma (HT29) cells were cultured in DMEM (Sigma Aldrich) with 10% fetal bovine serum at 37°C with 5% CO_2. A glass bottom dish was functionalized with collagen type I solution (100μg/mL) for 30 minutes at 37°C. The cells were plated on a glass bottom dish and fixed with 4% paraformaldehyde in PBS for 30 minutes prior to the imaging, which is performed in L-15 (Sigma Aldrich) with 30% fetal bovine serum to ensure the same optical properties of the media.

In order to control the environment while imaging live cells, an incubator (XL S1 W/CO2 kit, Zeiss) and a heating insert (P S1/Scan stage, Zeiss) were used.

g. WDT imaging for an extended time period

In order to show the capability of long-period measurement of WDT, here we show the result from imaging a HeLa cell using WDT. HeLa cells are prepared in a 35mm glass bottom dish (MatTek, P35G-1.0-14-C, uncoated) with Eagle's minimum essential medium (EMEM, ATCC, 30-2003) mixed with 10% fetal bovine serum (FBS, ATCC, 30-2020). This dish is then kept in the incubator (37°C, 5% CO_2) in order for the cells to adhere to the dish and settle. Throughout imaging, the same environment is provided to the sample using the incubator (XL S1 W/CO2 kit, Zeiss) and a heating insert (P S1/Scan stage, Zeiss).
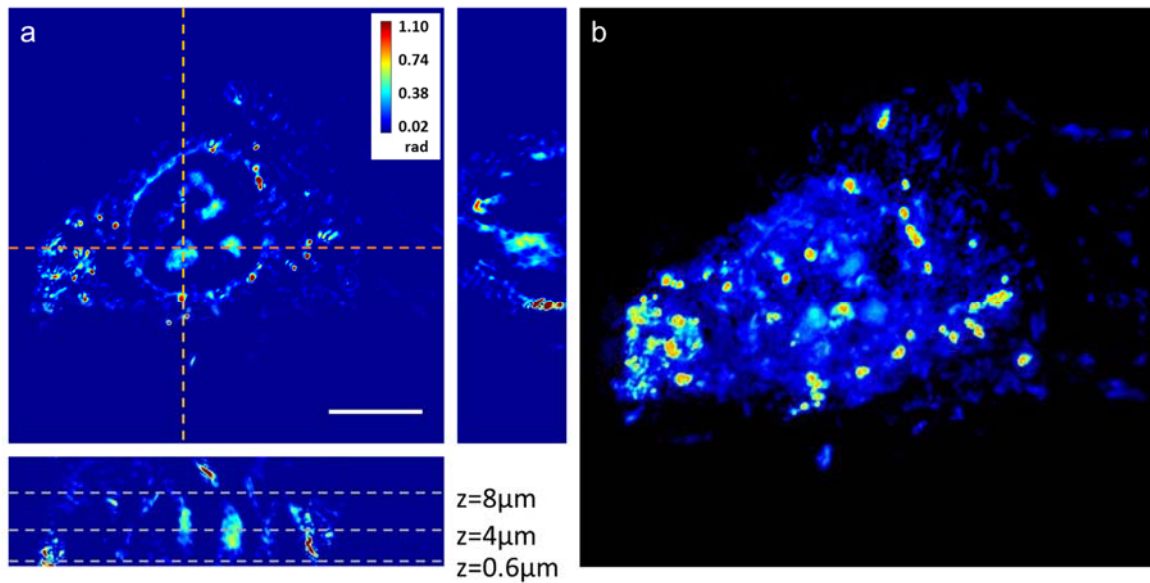
Figure S4. WDT reconstruction of a HeLa cell measured at 2 hours into the measurement over extended period of time. (a) z-stack after the reconstruction represented by its sections: (center) *x-y* plane taken at *z* = 4 μm from the bottom of the cell, (right) *y-z* section taken at the orange dashed line indicated on the center figure, (bottom) *x-z* section taken at the red dashed line indicated on the center figure. (b) 3D rendering of the same z-stack (Media S1). The scale bar in indicates 10 μm in sample plane.

SLIM measurement was performed every hour, taking a z-stack of 100 quantitative images each separated by 0.2 μm in depth. Figure S4a shows a z-stack taken at 2 hours into the measurement, represented by its sections through *x*, *y*, and *z*. This z-stack is then rendered using ImageJ 3D project module to record a 360° rotation of the cell in 3D (Fig. S4b). The same measurement process was taken place every hour, capturing the cell over time for 24 hours. Importantly, the HeLa culture was kept on the stage of the microscope during this 24 hour period without being disturbed or dying because of the well-controlled environment. Figures S5, S6 and S7 show the images over time, taken at certain z-positions (indicated in the bottom figure of Fig. S4a) from 25 separate z-stacks. Notice that for each of these images, we can observe active movements of the cell, and even the increase in the number of nucleoli, which indicates the viability of the cell under this environment, therefore the capacity of WDT imaging over an extended period of time.
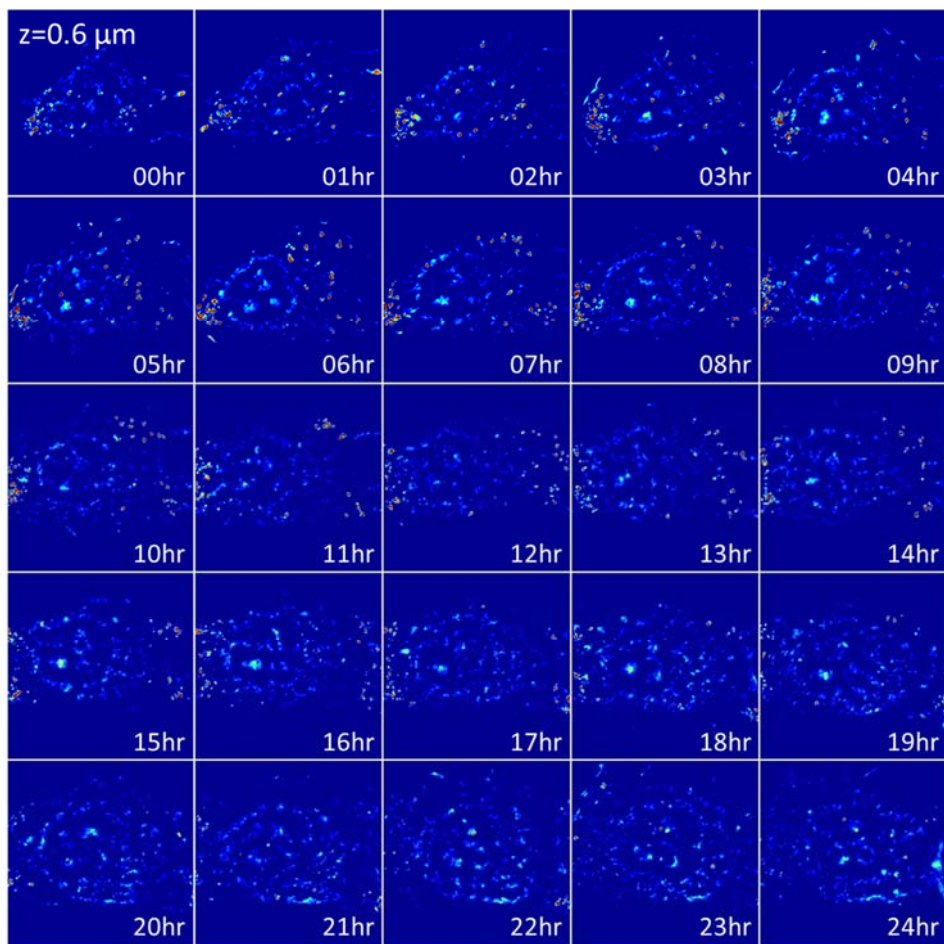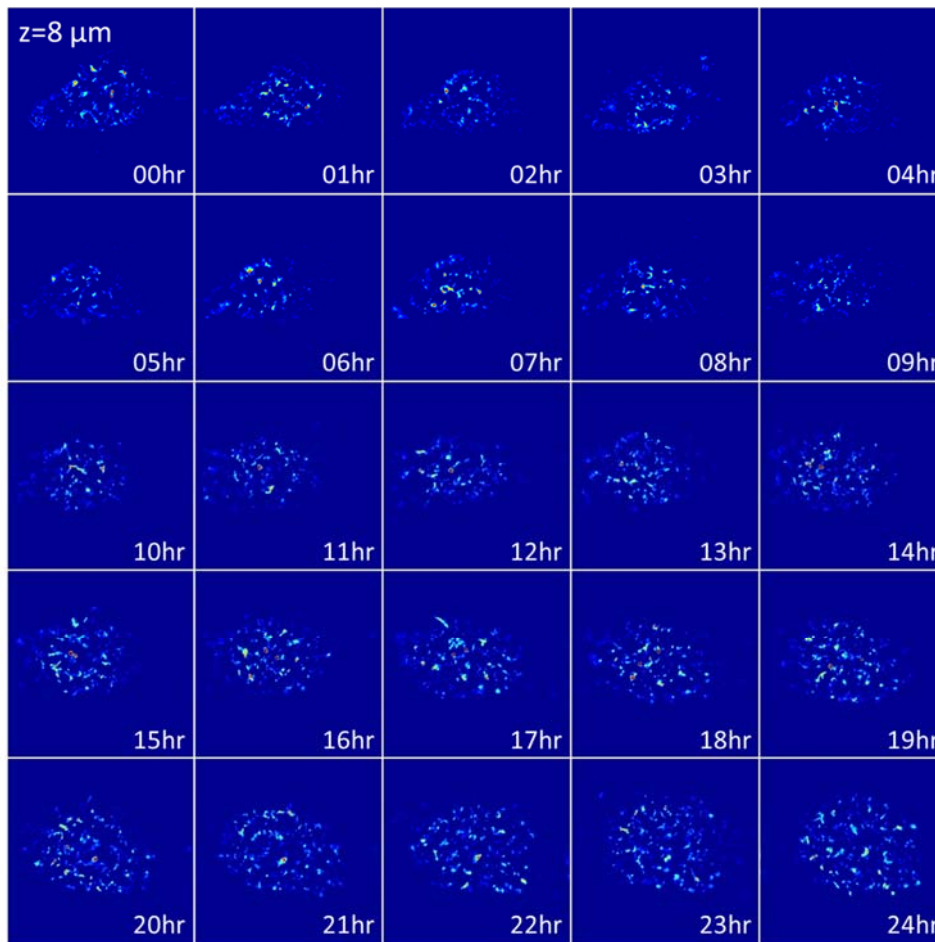
Figure S5. WDT image of HeLa cell shown by its *x-y* section taken at z = 0.6 μm from the bottom of the cell, where the bottom of the cell membrane and spiculate structure around it is shown. Each of the 25 images shares the same field of view as Fig. S4a and also the color bar.
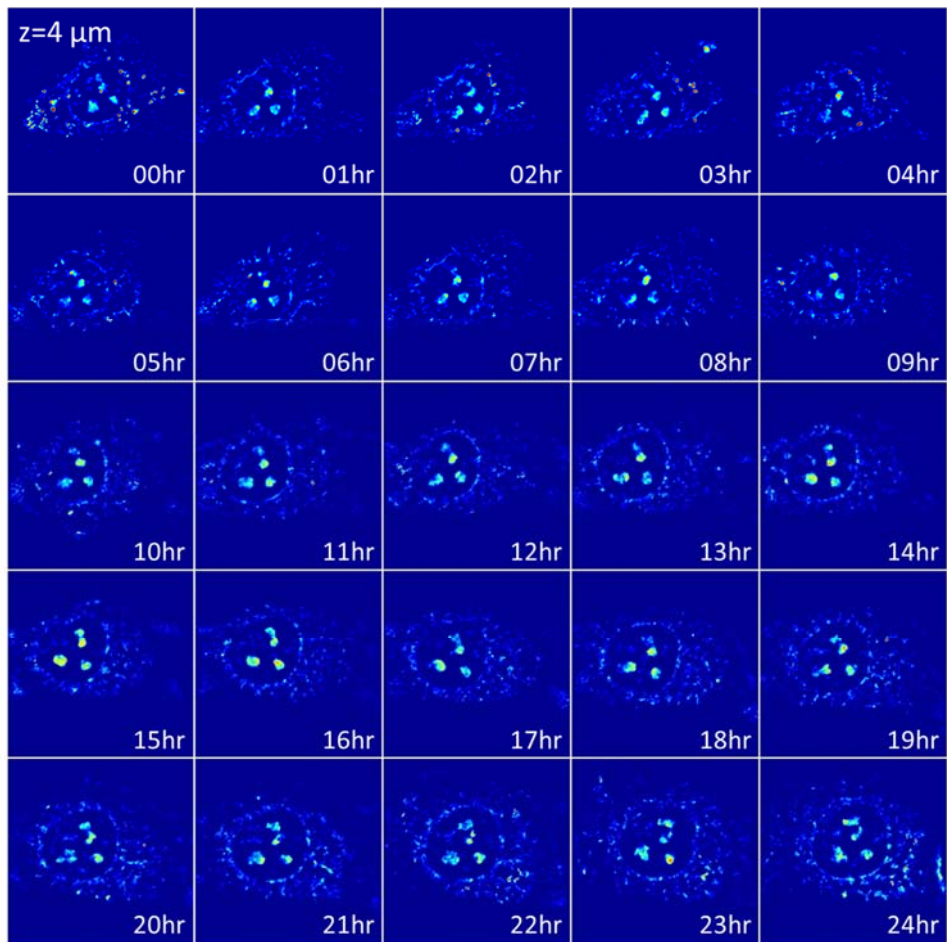
Figure S6. WDT image of HeLa cell shown by its *x-y* section taken at z = 4 μm from the bottom of the cell, where the nucleoli is clearly shown. Increase in the number of nucleoli shows that the cell is in a proper environment to grow and is in the process of division. Each of the 25 images shares the same field of view as Fig. S4a and also the color bar.

Figure S7. WDT image of HeLa cell shown by its *x-y* section taken at z = 8 μm from the bottom of the cell, where the top of the cell membrane is shown. Each of the 25 images shares the same field of view as Fig. S4a and also the color bar.

h. WDT imaging of 1 μm polystyrene microbeads

1 μm polystyrene beads (Thermo Scientific™ 5000 Series Polymer Particle Suspensions, 5100A. n_b = 1.59) immersed in microscope objective immersion oil (n_o = 1.516) is imaged using WDT. The sample is prepared by drying the aqueous suspension of 1μm polystyrene beads to evaporate the water on a glass cover slip, and then re-suspending the dry beads by applying the immersion oil on top of the dry beads, which is then covered by another cover slip. WDT imaging is done with 60 ms exposure time and 200 nm step size between each slice for 128 slices. The images are then reconstructed into quantitative phase images, and deconvolved using the PSF calculated using the WDT theory in order to obtain a quantitative phase tomogram. The phase tomogram is then converted to show the height, *h*, of the sample using the equation, $h = \lambda \Delta\phi / 2\pi(n_b - n_o)$, where λ is the mean illumination wavelength and $\Delta\phi$ is the measured quantitative phase shift. Figure S8 shows the reconstructed tomogram of the bead sample, where we can clearly see two beads in a different z-plane. Figures S8a and S8b show two different focal positions that are 1.6 μm (8 slices) away from each other, where each of the two beads is in focus. Figures S8c is the resliced view of

the bead on the top left of Fig. S8a, and Fig. S8d is the resliced view of the bead on the bottom right of Fig. S8b. After the deconvolution, the longitudinal FWHM of the bead in Fig. S8d is 1.27 μm, which is much less than the sum of the size of the bead (1 μm) and the width of the PSF of the system (0.89 μm). The elongation is expected since the axial resolution is 2.6X worse compared with the transverse resolution (350 nm in transverse vs. 890 nm in axial for WDT system).
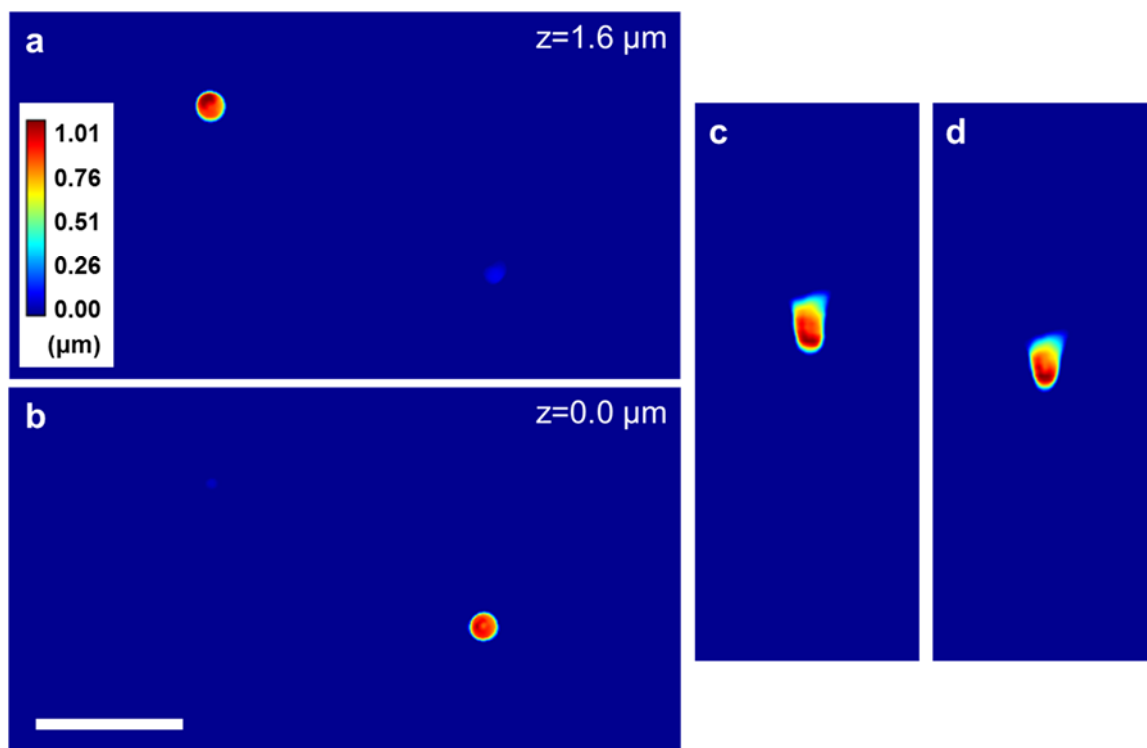

Figure S8. WDT tomogram of 1 μm polystyrene beads immersed in microscope objective immersion oil. (a) Quantitative height image at the focal position where the bead at top left corner of the field of view is in focus. The maximum height measured on the bead is 1.01 μm. (b) Quantitative height image at the focal position where the bead at the bottom right corner of the field of view is in focus. The maximum height measured on the bead is 0.95 μm. (c) Resliced image of the bead at the top left corner of (a). The longitudinal width of the bead is measured to be 1.32 μm and the transverse width is 0.97 μm. (d) Resliced image of the bead at the bottom right corner of (b). The longitudinal width of the bead is 1.27 μm and the transverse width is 0.94 μm. The scale bar indicates 5 μm in the sample plane.

i. Effect of dispersion introduced by a red blood cell

It is well known that hemoglobin (Hb) absorbs in the blue region of the visible spectrum. Here we investigate the effect on the WDT operation of this absorption and, thus, dispersion introduced by red blood cell (RBC) samples. From the refractive indices of H_2O[16], Hb[17], and human plasma[18, 19], the phase shift through an RBC with 2 μm thickness can be calculated as a function of radial frequency, ω. Using the molar extinction coefficient of Hemoglobin[20], the transmission amplitude through the cell can be calculated as well,. Figure S9 shows the phase shift, $\Delta\phi(\omega)$, and transmission amplitude, $|t(\omega)|$, for a RBC of typical thickness of 2 μm.
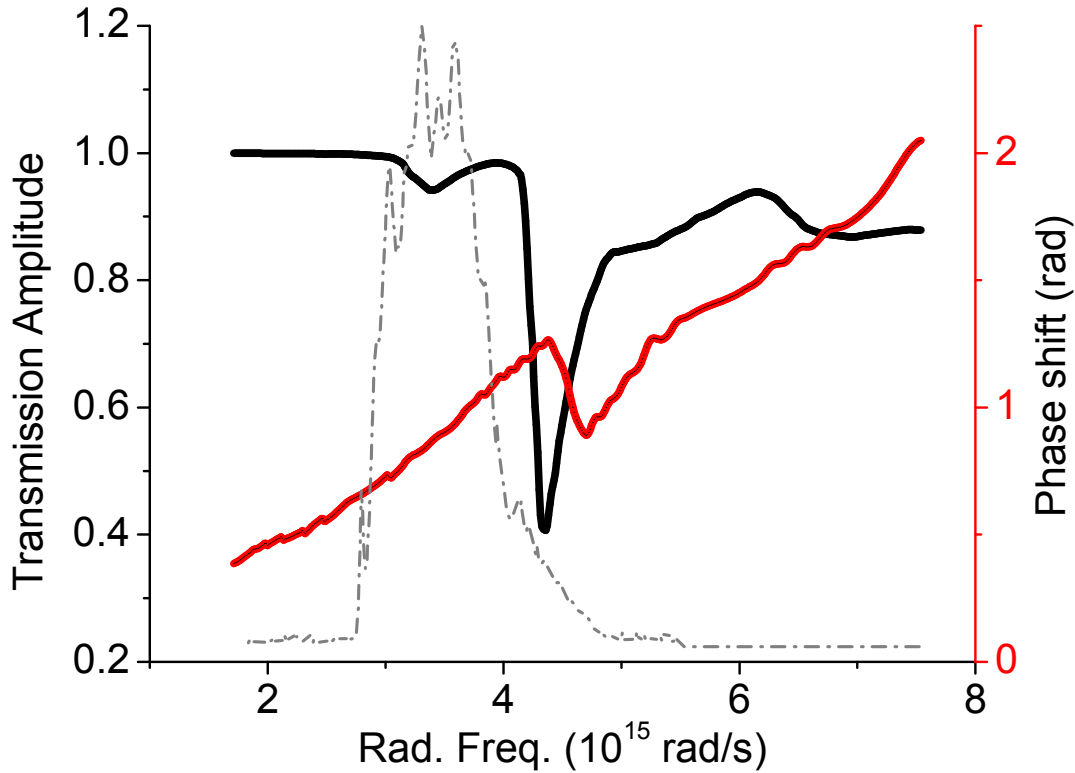
Figure S9. Transmission amplitude, $\left|t(\omega)\right|$, (black) and phase shift, $\Delta\phi(\omega)$, (red) through an RBC with 2 μm thickness. SLIM spectrum (gray) is overlaid to indicate the effective radial frequency range.

The complex transmission function through a RBC can then be represented as $t(\omega)=\left|t(\omega)\right|e^{i\Delta\varphi(\omega)}$. To quantitatively analyze the effects of $t(\omega)$ onto the PSF of WDT, we note that this function affects the cross-spectral density, W_{12}, via a multiplication operation, namely, $W_{12}{}'(\mathbf{k}_\perp,z,\omega)=t(\omega)W_{12}(\mathbf{k}_\perp,z,\omega)$. This procedure has been used for studying dispersion effects in low-coherence interferometry (see, e.g., Section 7.2. in Ref. [21]).
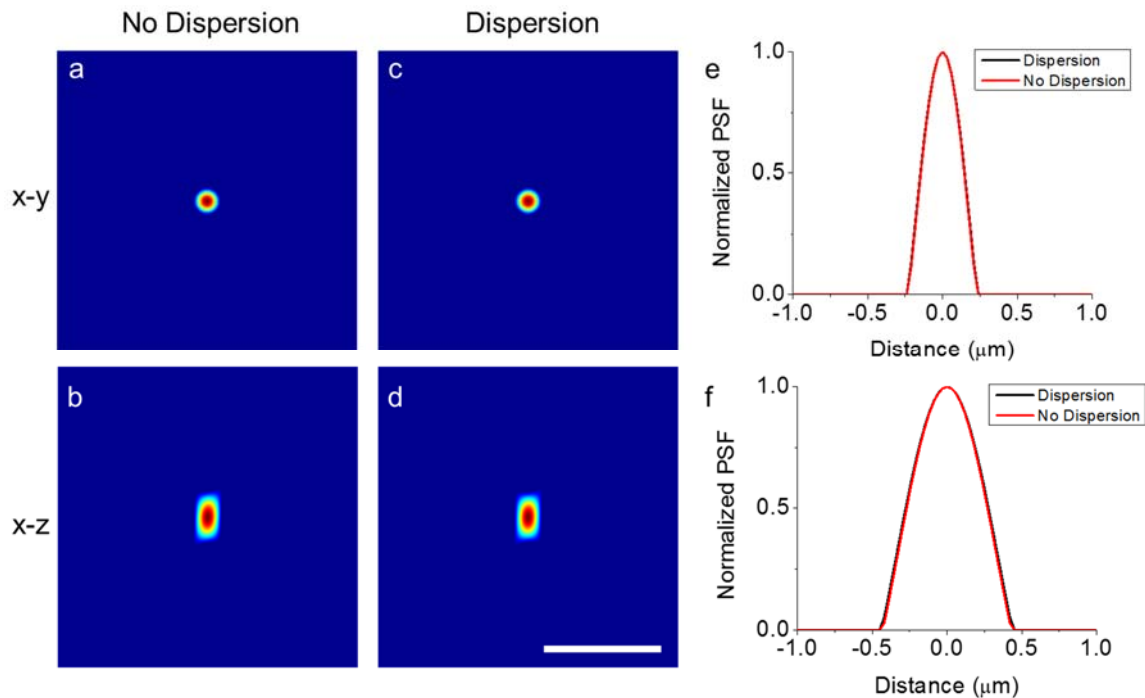
The cross-correlation function in Eq. (b14) becomes,

$$\Gamma_{12}\left(\mathbf{k}_\perp,z;0\right)=\frac{1}{8\bar{n}^2}\int_0^\infty \frac{\left(Q^2+k_\perp^2\right)^2}{Q^3}S'\left(-\frac{Q^2+k_\perp^2}{2Q}\right)\chi\left(\mathbf{k}_\perp,Q\right)e^{izQ}dQ$$

$$=\frac{1}{8\bar{n}^2}FT_Q^{-1}\left[\frac{\left(Q^2+k_\perp^2\right)^2}{Q^3}S'\left(-\frac{Q^2+k_\perp^2}{2Q}\right)\right]\circledv_z\chi\left(\mathbf{k}_\perp,-z\right), \qquad \text{(i1)}$$

$$=\Sigma'\left(\mathbf{k}_\perp,-z\right)\circledv_z\chi\left(\mathbf{k}_\perp,-z\right)$$

where $S'(\omega) = t(\omega)S(\omega)$. Taking the Fourier transform with respect to z, we obtain the modified version of Eq. (b15),

$$\Gamma_{12}(\mathbf{k}_\perp, Q; 0) = \Sigma'(\mathbf{k}_\perp, Q)\chi(\mathbf{k}_\perp, Q) \qquad (i2)$$

where

$$\Sigma'(\mathbf{k}_\perp, Q) = \frac{1}{8\bar{n}^2} \frac{\left(Q^2 + k_\perp^2\right)^2}{Q^3} S'\left(-\frac{Q^2 + k_\perp^2}{2Q}\right) \qquad (i3)$$


Figure S10. Comparison between the calculated PSF with and without dispersion. (a) and (b) Calculated PSF when there is no dispersion shown in the transverse and longitudinal direction, respectively. (c) and (d) the calculated PSF when there is dispersion effect on the sample shown in the transverse and longitudinal direction, respectively. (e) Horizontal profile through the center of the PSF in (a) and (c). (f) Vertical profile through the center of the PSF in (b) and (d). The scale bar corresponds to 2 μm.

Based on Eq. (i3), we compute the new PSF of the system, which now includes the effect of RBC dispersion and absorption. Figure S10 shows the cross-sections of calculated PSFs for the case without dispersion, S10a and S10b, and for the case with dispersion, S10c and S10d. To be consistent with the measurements, we applied threshold to the calculated PSF. Also, Fig. S10e and S10f show the transverse and longitudinal profiles through the center of the PSF, respectively.

The two PSFs are almost identical, with a very slight broadening caused by the dispersion. In the transverse dimension (Fig. S10e), the FWHM of the PSF with dispersion is 0.272 μm, while the FWHM of the case without dispersion is 0.268 μm. In the longitudinal dimension (Fig. S10f), the FWHM of the PSF with dispersion is 0.510 μm, while the FWHM of the case without

dispersion is 0.499 μm. Therefore, we can conclude that the dispersion and absorption in single red blood cells has a negligible effect on the overall performance of the WDT system.

This weak effect of dispersion through a RBC is expected. Since the illumination spectrum of the SLIM system only covers the radial frequency range roughly from 3.0×10^{15} rad/s to 4.0×10^{15} rad/s with considerable intensities, the effect of dispersion through an RBC can be limited to the same range as shown in Fig. S11. It can be seen that the transmission is fairly flat, while the spectral phase is essentially linear. Therefore, the transmission function of the RBC can be represented in the form of $t(\omega) = |t(\omega)| e^{i\alpha\omega}$ where $|t(\omega)| \approx 1$ and $\alpha\omega$ is the linear phase shift.

Since the linear phase shift does not change the shape of the cross-correlation function, but just shifts it in time. Therefore, we can conclude that the dispersion through a RBC has negligible effect on the entire imaging system.
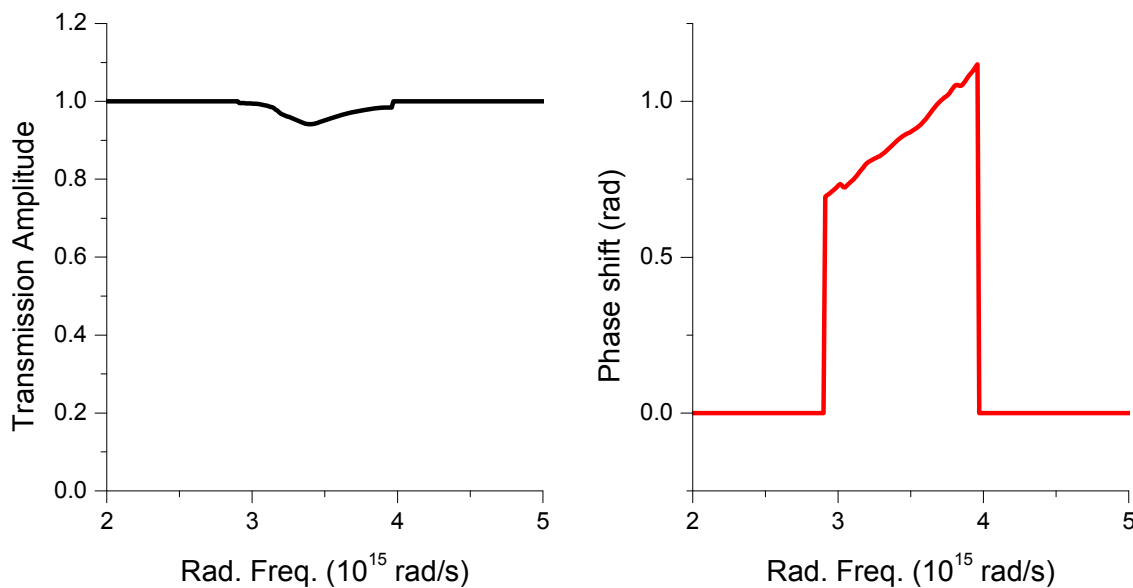
Figure S11. Transmission amplitude and phase shift through a 2 μm RBC in the SLIM spectrum window.

j. Point spread function vs. numerical aperture in WDT

Another method to assess the validity of WDT is to see the relationship between the resolution and the numerical aperture (NA). In order to do so, point spread function (PSF) for many different values of numerical aperture is calculated. Figure S12a shows the point spread functions in x-z plane, numerically calculated using WDT theory for various NA values ranging from 0.1 to 2. It is clear that for higher NA, the resolution is higher not only in the transverse dimension, but also in the longitudinal dimension. Figure S12b shows the linear relationship between the transverse resolution and inverse NA, and Fig. S12c shows the linear relationship between the longitudinal resolution and inverse NA squared. From this assessment, it is clear to say that WDT successfully model the light scattering.
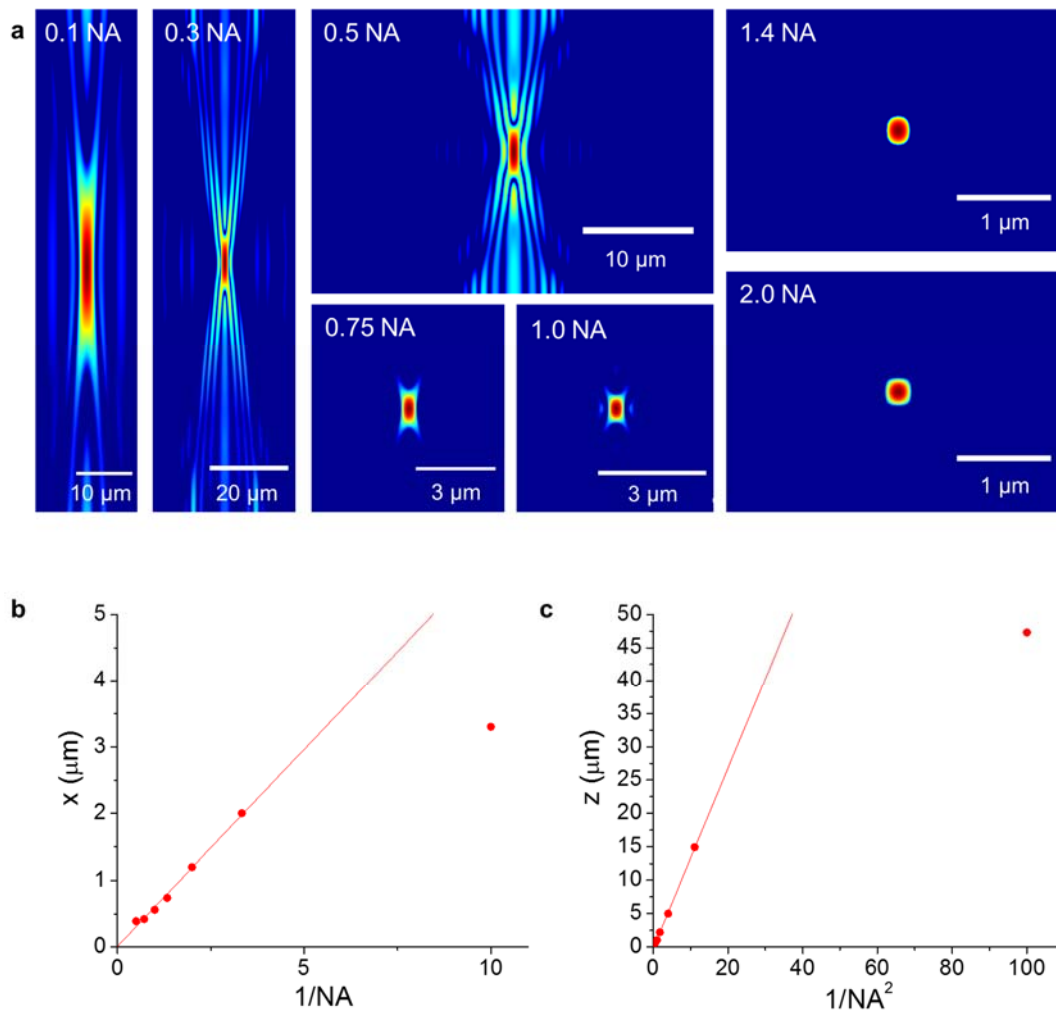
Figure S12. Point spread function calculated for various numerical aperture of the objective lens. (a) Point spread function for NA values ranging from 0.1 to 2, and shown in x-z plane. NA used for calculation and also the scale bars are indicated for each PSF separately. (b) Plot of transverse resolution as a function of inverse NA, where it clearly shows a well-defined linear relationship for most NA values. (c) Plot of longitudinal resolution as a function of inverse NA squared. It is clearly shown that the longitudinal is proportional to inverse NA squared.

References

1.   Wang, Z*., et al.* Spatial light interference microscopy (SLIM). *Optics Express* **19**, 1016 (2011).

2.   Wang, Z*., et al.* Topography and refractometry of nanostructures using spatial light interference microscopy. *Optics Letters* **35**, 208-210 (2010).

3.   Mir, M*., et al.* Visualizing Escherichia coli Sub-Cellular Structure Using Sparse Deconvolution Spatial Light Interference Tomography. *PLoS ONE* **7**, e39816 (2012).

4.   Mir, M*., et al.* Optical measurement of cycle-dependent cell growth. *Proceedings of the National Academy of Sciences* **108**, 13124-13129 (2011).

5.   Wang, Z*., et al.* Label-free intracellular transport measured by Spatial Light Interference Microscopy. *J. Biomed. Opt.* **16**, 026019 (2011).

6.   Wang, R*., et al.* Dispersion-relation phase spectroscopy of intracellular transport. *Optics Express* **19**, 20571-20579 (2011).

7.   Mir, M., Tangella, K. & Popescu, G. Blood testing at the single cell level using quantitative phase and amplitude microscopy. *Biomedical optics express* **2**, 3259-3266 (2011).

8.   Wang, Z., Popescu, G., Tangella, K.V. & Balla, A. Tissue refractive index as marker of disease (Journal Paper). *Journal of Biomedical Optics* **16**, 116017 (2011).

9.   Sridharan, S., Mir, M. & Popescu, G. Simultaneous optical measurements of cell motility and growth. *Biomedical optics express* **2**, 2815-2820 (2011).

10.   Wiener, N. Generalized harmonic analysis. *Acta Mathematica* **55**, 117-258 (1930).

11.   Khintchine, A. Korrelationstheorie der stationären stochastischen Prozesse. *Mathematische Annalen* **109**, 604-615 (1934).

12.   Donoho, D.L. For most large underdetermined systems of linear equations the minimal *Communications on pure and applied mathematics* **59**, 797-829 (2006).

13.   Szameit, A*., et al.* Sparsity-based single-shot subwavelength coherent diffractive imaging. *Nature materials* (2012).

14.   Shechtman, Y., Eldar, Y.C., Szameit, A. & Segev, M. Sparsity based sub-wavelength imaging with partially incoherent light via quadratic compressed sensing. *Optics Express* **19**, 14807-14822 (2011).

15.   Babacan, S.D., Molina, R. & Katsaggelos, A.K. Sparse Bayesian image restoration. in *17th IEEE International Conference on Image Processing (ICIP)* 26-29 (2010).

16.   Daimon, M. & Masumura, A. Measurement of the refractive index of distilled water from the near-infrared region to the ultraviolet region. *Applied Optics* **46**, 3811-3820 (2007).

17.   Friebel, M. & Meinke, M. Model function to calculate the refractive index of native hemoglobin in the wavelength range of 250-1100 nm dependent on concentration. *Applied Optics* **45**, 2838-2842 (2006).

18.   Vörös, J. The Density and Refractive Index of Adsorbing Protein Layers. *Biophysical journal* **87**, 553-561 (2004).

19.   Adair, G.S. & Robinson, M.E. The specific refraction increments of serum-albumin and serum-globulin. *Biochemical Journal* **24**, 993 (1930).

20.   Kim, T., Sridharan, S. & Popescu, G. Fourier Transform Light Scattering of Tissues. in *Handbook of Coherent-Domain Optical Methods* (ed. V.V. Tuchin) 259-290 (Springer, New York, 2013).

21.   Popescu, G. *Quantitative phase imaging of cells and tissues* (McGraw Hill, 2011).